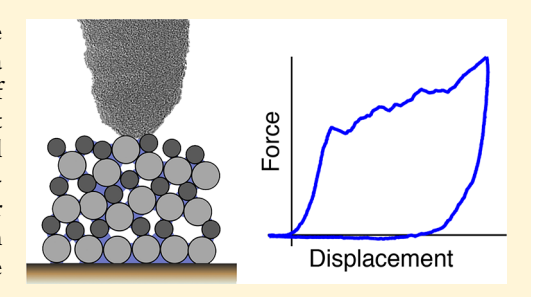
Downloaded by UNIV OF PENNSYLVANIA at 06:07:55:305 on June 22, 2019 from https://pubs.acs.org/doi/10.1021/acs.nanolett.8b01640.

Disordered Nanoparticle Packings under Local Stress Exhibit Avalanche-Like, Environmentally Dependent Plastic Deformation

Joel A. Lefever, ^{†,∞} Jason P. Mulderrig, [‡] Jyo Lyn Hor, ¶ Daeyeon Lee, ¶ and Robert W. Carpick*, §

Supporting Information

ABSTRACT: Nanoindentation experiments on disordered nanoparticle packings performed both in an atomic force microscope and in situ in a transmission electron microscope are used to investigate the mechanics of plastic deformation. Under an applied load, these highly porous films exhibit load drops, the magnitudes of which are consistent with an exponential population distribution. These load drops are attributed to local rearrangements of a small number of particles, which bear similarities to shear transformation zones and to the T1 process, both of which have been previously predicted for disordered packings. An increase in the relative humidity results in an increase in the number of observed load drops,



indicating that the strength of the particle interactions has a significant effect on the modes of plastic deformation. These results suggest how disordered nanoparticle packings may be expected to behave in devices operating under varying environments. KEYWORDS: Granular material, in situ TEM, atomic force microscopy, nanoindentation, layer-by-layer, capillary condensation, porous materials

he plastic deformation mechanisms of disordered materials, including nanoparticle packings, remain poorly understood and difficult to predict despite extensive research efforts. 1-3 With a more complete understanding of their mechanical properties, disordered nanoparticle packings will be promising in numerous commercial applications, including optical coatings,⁴ solar cells,⁵ and nanoprinting.⁶ In many of these applications, nanoparticle packings may benefit from a tunable index of refraction⁷ and excellent processability which allows the materials to adapt to unusual geometries, including flexible substrates.⁶ In addition, they serve as a useful model system for investigating the plastic deformation of disordered materials in general.8 For example, diamond-like carbon (DLC) and metallic glass, which are important for many applications, 9-11 are two classes of disordered materials which could potentially be modeled in this way. The longevity and durability of applications involving these materials may be improved if the modes of plastic deformation are more fully understood. Furthermore, the ambient humidity can affect the strength of interparticle bonds in disordered nanoparticle packings, but the attendant effects on the mechanical strength of the packings is not understood. 12 Therefore, it is also important to investigate how the plasticity of the film is affected by environmental conditions. 13

Disordered materials are known to feature some population of locally soft spots. These soft spots can manifest themselves

as regions of a few atoms or particles with low-frequency vibrational modes, high energy dissipation, 4 or mechanically soft or compliant regions.8 Under an applied stress, these regions may rearrange, either in the form of a shear transformation zone (STZ) in which several constituents cooperatively rearrange, 15,16 or via a T1 process in which a single constituent moves to occupy previously empty volume without disturbing its neighbors.¹⁷ Each of these modes of plastic deformation leaves behind no obvious trace of their occurrence, and must be treated as a discrete event. In order to be studied, these events must be observed or captured in action, unlike a dislocation which may be observed post mortem. Furthermore, it is even more difficult to distinguish between these two modes of deformation, and some rearrangements could be a hybrid of the properties of an STZ and a T1 process, as we will discuss later.

Current research suggests that many disordered materials share similarities in their modes of plastic deformation. 13,18-20 Amorphous materials of many types and spanning many length scales have been recently shown to exhibit comparable yield strains, ¹³ with the spatial extent of STZs on the order of a few constituent particle diameters. ^{16,21} The magnitudes of the force

Received: April 23, 2018 Revised: August 7, 2018 Published: August 13, 2018



[†]Department of Materials Science & Engineering, University of Pennsylvania, Philadelphia, Pennsylvania 19104, United States [‡]Department of Mechanical and Aerospace Engineering, Princeton University, Princeton, New Jersey 08544, United States

[¶]Department of Chemical & Biomolecular Engineering, University of Pennsylvania, Philadelphia, Pennsylvania 19104, United States

[§]Department of Mechanical Engineering & Applied Mechanics, University of Pennsylvania, Philadelphia, Pennsylvania 19104, United States

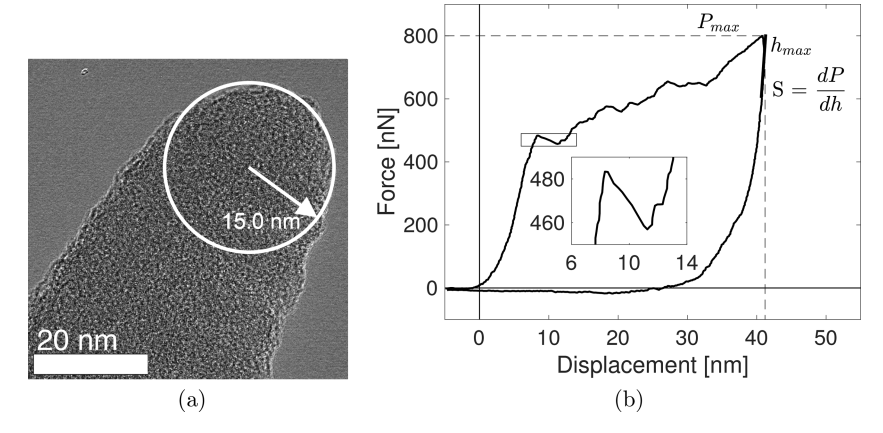


Figure 1. (a) Transmission electron micrograph of one of the DLC-coated AFM probes used in this study, with the circle of best fit plotted. The radius of this circle was used in evaluating the area in contact. (b) Example of a force curve with the stiffness S used in determining the modulus denoted. Several load drops are also visible as serrations in the approach portion of the curve; one is shown in the inset.

and displacement relaxations during rearrangements in disordered materials are often modeled using avalanche theory, which predicts that the magnitudes of slip or rearrangement events follow a power law probability distribution. This scaling is seen to apply across many material systems. However, it remains an open research question to determine how the environment and composition of these materials affect their mechanical response.

An important environmental consideration that can substantially affect the performance of nanoparticle packings is humidity. 25,26 For example, in a previous study, an increase in humidity was seen to result in enhanced stiffness and hardness of a nanoparticle superlattice.²⁷ However, the relative humidities that were explored were relatively dry (\leq 35%), and controlled indirectly via temperature. In experiments on disordered colloidal packings, an increase in relative humidity was found to increase the total energy dissipated upon compression, which suggests that humidity enhances plastic deformation.¹³ Molecular dynamics simulations have demonstrated that the forces exerted by capillary bridges between a pair of spherical nanoparticles are weakest at relative humidity levels above 80% and below 10%; the forces are greatest in the intermediate range.¹² In addition, at high humidity levels, it is possible to form capillary bridges between particles even at greater separation distances, so the range over which the capillary force can act is increased.12

Although simulations have extended the analysis of capillary-mediated interactions to two-dimensional disordered granular packings, ²⁸ the effect of relative humidity on the deformation mechanisms of a disordered nanoparticle packing, to our knowledge, has not been investigated experimentally. In addition to changing the interparticle bonding via capillary bridge formation, ^{25,29} humidity may also affect the propensity to form hydrogen bonds or covalent metal oxide bonds between nanoparticles. ^{30,31} As such, humidity control offers a convenient means to tune the interactions between neighboring particles, which may further enhance the use of nanoparticle packings as model systems for other types of disordered materials including metallic glasses, which are more strongly bonded due to interatomic interactions, and granular packings, which are far more weakly bonded and often purely repulsive.

Nanoindentation experiments have been used previously to search for defects in metallic glass^{32–34} and nanoparticle

packings.^{2,8} In our previous work,⁸ we used nanoindentation techniques to study the mechanical properties of singlecomponent silica nanoparticle packings which were produced by spin-coating.⁴ In this paper, we use nanoindentation techniques to investigate the effect of humidity on the mechanical properties of two-component disordered nanoparticle packings which have been deposited using layer-bylayer (LbL) deposition. This deposition technique produces films which have a lower packing fraction than those created by spin-coating. Due to the lower packing fraction in this material, the rearrangements that occur are more prominent and more readily quantified than those observed previously in spincoated films.8 This paper will demonstrate that capillary condensation alters the mechanical properties of disordered nanoparticle packings. In addition, it will examine the distribution of the sizes of the rearrangements that occur.

Disordered nanoparticle packings were produced by LbL deposition of titania and nanodiamond nanoparticles. The anatase titania nanoparticles (US Research Nanomaterials, Houston, TX) had a diameter of 5-15 nm, while the nanodiamond (RT-DND-SP, Ray Techniques Ltd., Jerusalem, Israel) had a diameter of 3.5-5.5 nm. The titania nanoparticle suspension was adjusted from the stock concentration of 15 wt % to a concentration of 0.05 wt %, and the pH was adjusted to 3 by adding 1 M hydrochloric acid solution. The nanodiamond suspension was also adjusted from the stock concentration of 5 wt % to a concentration of 0.05 wt %, and the pH was adjusted to 4. These pH levels were selected to facilitate LbL deposition: the pH of the two suspensions must be chosen carefully to prevent bound nanoparticles from being released into the suspension while still maintaining opposite charges between the two species.^{35,36} In the case of these two specific solutions, exactly matching the pH induces aggregation in one or the other species as they become un-ionized near their isoelectric points. The LbL deposition process was performed to produce 20 bilayers on a 650 μ m wide silicon substrate. AFM topography measurements over the edge of the film revealed that the film was 166 ± 18 nm thick. The single crystal silicon substrate (Hysitron, Inc., Eden Prairie, MN) included a wedge-shaped region which facilitates in situ observation via transmission electron microscopy (TEM). TEM (2010F, JEOL Ltd., Tokyo, Japan) confirmed that the films were disordered, which was also evident in the topography images taken via atomic force microscopy (AFM).

The mechanical properties of the film were evaluated by performing nanoindentation in an AFM (Icon, Bruker, Boston, MA) using a tapping-mode cantilever with a DLC coating (Tap300DLC, BudgetSensors, Sofia, Bulgaria). A fixed maximum load of 800 nN was used in every experiment. This maximum load was chosen to prevent probe fracture which occurs at higher loads. The radius of the AFM probe was determined using TEM³⁷ and the condition of the probe was checked before and after every experiment. Experiments were discarded if the probe was severely damaged and no longer round. An example of an unused tip is shown in Figure 1a.

In our previous work, we used the Oliver–Pharr method to determine the reduced modulus of the tip/sample system E_r via

$$E_r = \frac{S\sqrt{\pi}}{2\beta\sqrt{A}}\tag{1}$$

where β is a dimensionless constant equal to 1 for a spherical probe, S is the slope of the initial part of the retract curve, shown in Figure 1b, and A is the contact area at the maximum load. 8,38,39 In the present study, however, load drops were prevalent, which significantly increased the indentation depth compared with a force-distance curve that exhibits no load drops. Because the indentation depth was frequently greater than the radius of the probe, the contact area could be assumed to be equal to the area of a circle with the same radius as the probe. However, this large-deformation approximation violates the assumptions of ref 39 which assumes that the indenter surface is nearly tangent to the substrate and that most of the deformation is normal to the substrate. Therefore, in the present paper we simply report the stiffness $S = \frac{dP}{dh}$ of the sample, as shown in Figure 1b. We will discuss later the approximate value of elastic modulus that would be measured if this assumption is accepted. For the same reason, instead of hardness, we will report indentation depth here. The energy dissipated in the course of an indentation experiment is the cyclic integral of load with respect to depth, $E_{diss} = \oint P \, dh$. Load drops were frequently observed in the force vs distance curves, as shown in Figure 1b. These were identified by searching for successive peaks and valleys using a custom MATLAB (MathWorks, Natick, MA) script. To distinguish load drops from instrumental noise, only load drops exceeding a minimum threshold of 10 nN were included in the analysis.

The humidity in the AFM chamber was varied by opening the chamber to reach ambient relative humidity (RH $\approx 40-55\%$), by flooding the chamber with a supply of dry nitrogen (RH ≈ 0), and by placing open dishes of nearly boiling water inside the sealed chamber. These conditions allowed us to reach relative humidity levels between 18% and 100%. The boiling water did not affect the temperature of the air inside the chamber by more than 2 °C. A hygrometer (Fisher Scientific, Waltham, MA) was used to measure the relative humidity. Topography scans were performed in tapping mode both before and after indentation to verify that the surface was uniform and to determine the deformation of the sample due to the indentation.

To investigate and eliminate the possibility of any hysteresis effects related to the formation of capillary bridges, we performed experiments at first under nearly saturated conditions, then incrementally reduced the humidity to ambient conditions, followed by dry, ambient, and saturated

conditions. The data obtained at high humidity are further divided into 98% and 100% conditions, for reasons to be discussed further below. With the exception of experiments performed near saturation, we saw no systematic change in measurements over 20 min after reaching a particular humidity level, so experiments were begun immediately after reaching the target humidity.

To provide another view of rearrangements, nanoindentation experiments were also performed *in situ* in a TEM, using a holder which facilitates mechanical testing (PicoIndenter, Hysitron, Inc., Eden Prairie, MN). Using this experimental setup, a sample prepared under the identical conditions but with 30 bilayers was used to ease visualization. The greater thickness provided visibility in the TEM. Experiments were performed on the wedge-shaped portion of the sample, using a cube-corner diamond punch with an end radius of approximately 200 nm.

We observe that the mechanical properties of the sample change with the relative humidity, as can be seen in Figure 2.

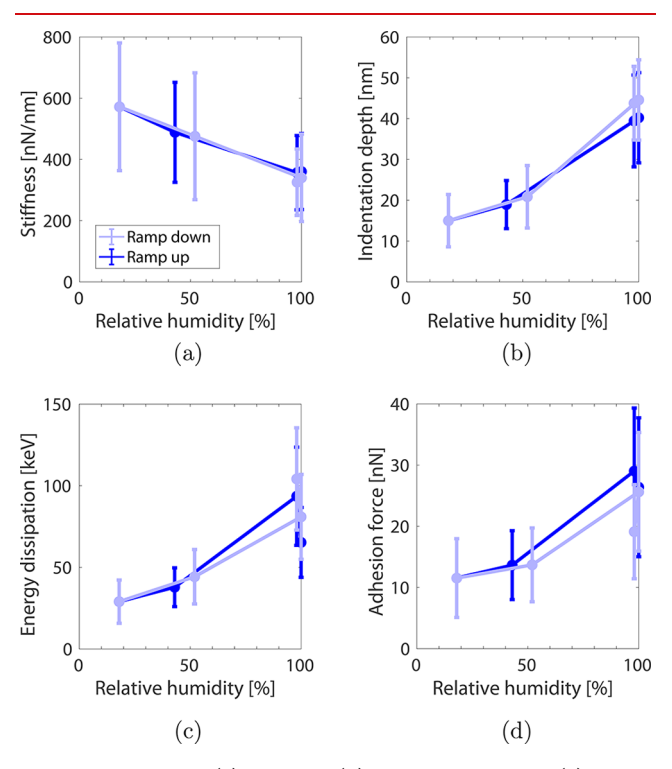


Figure 2. Measured (a) stiffness, (b) indentation depth, (c) energy dissipated, and (d) the pull-off force resulting from adhesion and capillary forces in the course of performing a nanoindentation experiment at various relative humidity levels. The error bars represent the standard deviation of the data set; because of the very large sample sizes, the differences between the various distributions are statistically significant with p < 0.05 in almost all cases. The connecting lines indicate the order in which the experiments were performed.

These results are numerically tabulated in Table 1, in the order the experiments were performed. The stiffness decreases with an increase in humidity, while the indentation depth and energy dissipation both increase. It is expected that the latter two effects are coupled; a greater indentation depth will necessarily result in more mechanical work. The fact that stiffness decreases concurrently with an increase in indentation depth would

Table 1. Contact Stiffness, Indentation Depth, and Energy Dissipation Each with Their Standard Deviations for Trials in the Order in Which They Were Performed^a

RH [%]	N	stiffness [nN/nm]	indentation depth [nm]	energy dissipation [keV]
98	36	326 ± 108	43.8 ± 9.0	104.2 ± 31.3
100	91	340 ± 143	44.6 ± 9.8	80.9 ± 26.0
52	170	476 ± 207	20.9 ± 7.6	44.3 ± 16.7
18	195	572 ± 209	15.0 ± 6.4	29.0 ± 13.2
43	197	489 ± 163	18.9 ± 5.9	37.8 ± 11.9
98	79	357 ± 121	39.4 ± 11.2	93.6 ± 30.1
100	67	360 ± 124	40.2 ± 11.0	65.3 ± 21.4

"N is the minimum number of indentation experiments evaluated at that humidity level. In some specific trials, the stiffness could not be evaluated, but the indentation depth and energy dissipation are still reported.

normally be expected to compact the sample further, which would stiffen the material if all other conditions were held constant.^{8,19}

The weakening of the particle—particle interactions both permits the sample to deform farther under a given load, and also to have a weaker restorative force or stiffness. Due to the sufficiently large sample sizes used here, the difference between the distributions of each parameter—stiffness, indentation depth, energy dissipation, and adhesion—under each set of environmental conditions is statistically significant with p < 0.05 (strong evidence of a difference) in almost all cases.

The gradual increase in the adhesion force shown in Figure 2d supports the hypothesis that the capillary structure is changing. This trend opposes the trend of decreasing adhesion force at very high humidity predicted in ref 12. The discrepancy may be attributed to the difference in the shape of the rough surface; it is possible to form capillary bridges with multiple particles rather than with just a single particle, and this is more likely to occur at higher humidity levels where the capillaries are generally larger. Verifying this idea requires further experiments and analysis that are beyond the scope of this paper.

The indentation depths are systematically greater in this study than in our prior study, which was conducted using nominally identical probes on a silica nanoparticle packing that was produced via spin coating. Therefore, all differences between the present behavior and the behavior witnessed previously may be attributed to the different materials used in each system. This observation, as well as the fact that indentation depth increases with humidity, may both be attributed to the load drops that are frequently visible in the force curves collected on this material system. These load drops appear as serrations in the force curve, as shown in Figure 1b, and more load drops are seen at high humidity than at ambient or dry conditions.

At every level of relative humidity we investigated, the distribution of the magnitudes of all load drops is roughly exponential, as shown in Figure 3. The dotted lines represent exponential fits to each data set. The decay length for each magnitude population distribution ranges from 9 to 20 nN, but this decay length has no clear, monotonic dependence on humidity. We speculate that this magnitude is nominally the same for all data sets, and the discrepancies observed here are due to random fluctuations in the data. We also note that the range of load drop magnitudes is constrained by avoiding low

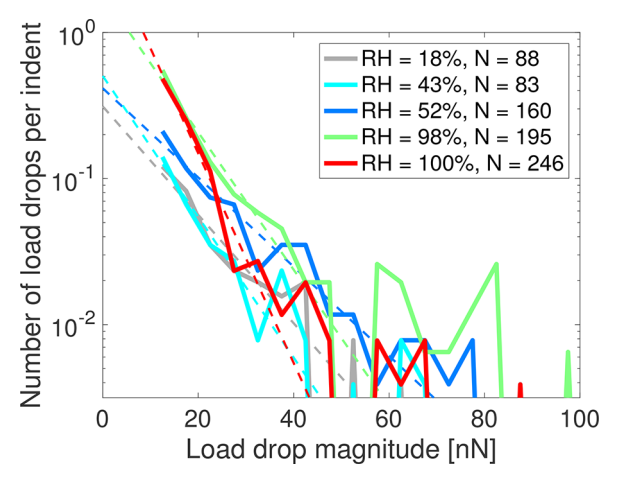


Figure 3. Histogram of the magnitude of load drops normalized by the number of indentation experiments performed. The distribution at each humidity level is roughly exponential, as shown by the dotted lines which are fits to the data. The total number of load drops observed under each condition is given in the legend. At 98% humidity, 154 indentation experiments were performed; at 100% humidity, 258 experiments were performed, and in all other cases, 256 experiments were performed. The number of experiments performed could not be held exactly equal due to experimental challenges.

magnitudes below 10 nN, as they could be attributable to noise, as mentioned above; load drops above 100 nN were very rarely observed in the 1280 experiments conducted. Given the distribution observed, improving the statistics above 100 nN would require orders of magnitude more experiments, which is not practical.

It is virtually impossible to maintain the humidity in the AFM chamber just below saturation for the extended duration needed to perform hundreds of indentation experiments without disturbing the apparatus. For this reason, we divide the data collected at high humidity into two categories. The data collected before reaching saturation is labeled as 98% in the figures and tables, and the data labeled as 100% are those collected after the AFM began showing signs of extended pulloff regimes characteristic of reaching a saturated capillary state. In particular, the capillary bridge between the film and the AFM probe can be sustained to a very large separation distance of several tens of nanometers, so a weak tensile force is sustained after the tip is no longer in contact with the particles themselves. An example of such a force curve is shown in the Supporting Information (Figure S2). The challenge associated with maintaining the humidity just below saturation is also responsible for the small sample size in these trials, as seen in Table 1. In practice, the humidity fluctuated by about 3% in every trial except when the humidity was at 100%. No discernible differences in mechanical properties were noted over a range of humidity of less than 3%, except in the case of going between 98% and fully saturated.

We observe a clear transition in behavior between a humidity of 98% and complete saturation. As the chamber reaches total saturation, more load drops occur at very low loads below 200 nN and fewer load drops occur at high loads above 400 nN. In addition, the force curves collected at 100% humidity suggest that a capillary bridge forms between the tip and the sample which does not break until the AFM tip is tens of nanometers away. At such high humidity, the tip leaves a clearly visible track on the sample when traveling between indentation sites (Figure S3b), despite the applied normal load

being quite small, on the order of 80 nN. We suggest that once fully saturated, this packing loses some of its solid structure, weakening to a viscous, almost slurry-like state. An example topography scan collected while the system was at saturation is shown in the Supporting Information (Figure S3a). This abrupt transition is also our best confirmation of the accuracy of the hygrometer, which registered 100% humidity at approximately the same time as the transition occurred. In addition, fogging and accumulation of condensation on the glass window further substantiated the estimate that the AFM chamber reached saturation.

The load drops observed in the current LbL deposited disordered nanoparticle packing were never observed in our prior work on spin-coated silica nanoparticles.8 There are several important distinctions between the nanoparticle packings used in these two studies. These include the particle composition, polydispersity, deposition method, and particle geometry. Of these differences, most likely the deposition method has the largest impact, because LbL deposition results in a packing fraction that is below the random close-packed limit of 64%, which is in part due to the repulsive interactions between particles of the same composition. By contrast, the particle composition likely has minimal effect because all species investigated here and previously are hard relative to the properties of the packing as a whole. The titania and nanodiamond nanoparticles, being crystalline, have a somewhat rougher (i.e., faceted) geometry than the silica nanoparticles which are quite smooth and spherical. However, any effect related to particle roughness should strengthen the present packings when in fact we observe a new, weakening mode of plasticity occurring. Similarly, the bidispersity could contribute to a more densely packed film, 40 which should be less conducive to sudden load-drop events. Therefore, the reduction in packing fraction is the most obvious explanation for the observed enhancement in plasticity in the LbL nanoparticle films as compared with the spin-coated films.

Our observation of material weakening at high humidity stands in contrast with the findings of Gallego-Gómez et al.,2 in which conventional nanoindentation was performed on a colloidal superlattice. The authors of that study observed a lower elastic modulus and hardness at low humidity. However, their means of varying the humidity was to vary the temperature of the substrate, assuming that by doing so the water in the capillaries would evaporate. The lower modulus and hardness observed at low humidity may in fact be due to the greater temperature and greater thermal activation of mechanisms that allow particle rearrangements. In addition, their experiments were only able to reach only the dry and pendular states²⁵ of meniscus formation because they did not supply the chamber with an extra source of water vapor, whereas the present experiments reach the predicted funicular and capillary states.

According to theory, the uptake of water will result in a change in the shape of the menisci in the sample. We suggest that these menisci are the reason why a film which is more compact might also be less stiff. Under very humid conditions, the meniscus will transition from a pendular to a funicular or capillary state. The reduction in air—liquid interfacial area reduces the capillary force resulting from surface tension. Furthermore, capillarity most likely ceases to play a role as the particles become increasingly surrounded by condensed water, so the capillary pressure becomes uniform on all sides of each particle. A similar weakening of the interparticle forces was

previously observed in simulation, 12 although that simulation considered only a pair of particles. Therefore, the overall structure of a capillary bridge connecting multiple particles was not considered. A more thorough experimental treatment of capillary formation between many particles has been accomplished at the mesoscale by observing wetting of glass beads with diameters on the order of 300–500 $\mu \rm m.^{29}$ X-ray tomography revealed the shapes of the clusters of water bridges that formed, which transitioned from individual bridges to clusters, and finally a percolated network of capillary bridges. 26 Only the funicular and capillary states were observed in that study. However, the shapes of capillaries in a granular packing near saturation have been visualized in a two-dimensional simulation. 28

In LbL deposition, nanoparticles in each deposition step cannot form a dense monolayer atop an existing packing of nanoparticles due to electrostatic repulsion, and a packing fraction much lower than the random close packing limit of 64% is expected.³⁵ This stands in contrast to the spin-coated silica nanoparticle films we investigated previously,8 which were expected to be very near the close-packing limit. Despite the low packing fraction, the nanoparticle packings used here are in a mechanically stable state, because they do not deform under the low load of tapping-mode AFM, gravity, or the inertial forces that result from routine moving or positioning of the sample. However, the packing cannot be considered to be in the shear-jammed state, because the shear-jammed state implies that the packing is stable only under an applied stress, 41,42 which is absent in this system when the system is at rest. This system is in a loosely packed state, and stability is imparted in part due to friction and adhesion between nanoparticles. Although an in-depth investigation of porosity is outside the scope of the present study, the greater porosity in the present films nonetheless appears to have a significant influence on the modes of plasticity we observe.

The transition from the smooth yielding observed on silica nanoparticle packings to the load drops observed here suggests that the mechanism of deformation is different in these two materials. Fluid-cell ellipsometry and Rutherford backscattering experiments suggest that the porosity is much greater in LbL deposited films as compared with the spin-coated films investigated previously.8 The porosity is likely greater than 50%, although experimental difficulties prevent obtaining a precise value. As the silica nanoparticle films are nearly at the close-packing limit, their likely mode of plasticity is a cooperative rearrangement of many particles such as an STZ. 15,16 In contrast, the instantaneous yielding exhibited by the porous LbL films might exhibit behavior closer to a T1 process, which is a rearrangement primarily consisting of a single particle moving into a region of excess free volume. 17 Because the T1 process requires this free volume, it is more likely to occur in the porous film. Then as soon as a freestanding particle breaks loose from its neighbors, the force curve exhibits a load drop due to the collapse of the void

The roughly exponential distribution of load drops suggests that there is a characteristic load associated with plasticity in this system. From the exponential fits shown in Figure 3, this load is estimated to be between 9 and 20 nN. Previous studies on the distribution of relaxation events have generally suggested a power-law relationship rather than an exponential decay. ^{22–24} However, in the overdamped limit, an exponential decay is sometimes observed at the high-magnitude cutoff. ²⁴ A

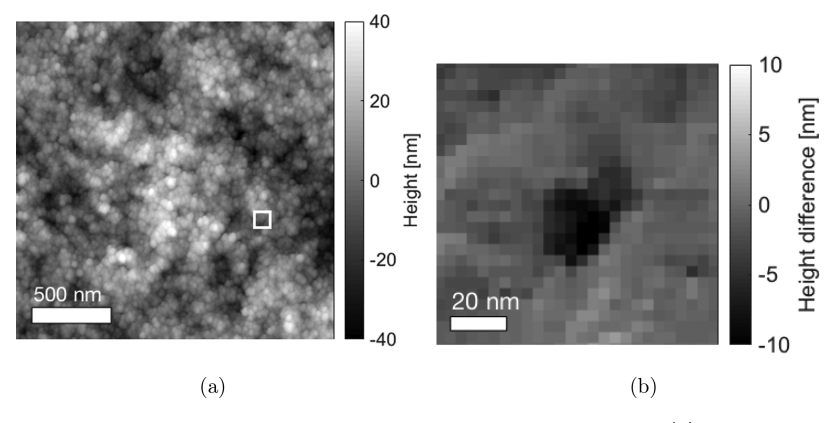


Figure 4. (a) Sample topography scan, taken prior to the experiments performed at 18% humidity. (b) Difference image; the topography after an indentation experiment has been subtracted from the topography prior to the indentation experiment. The disturbed region is approximately the area of a single particle, with no other particles disturbed. The region corresponds to the square in part a.

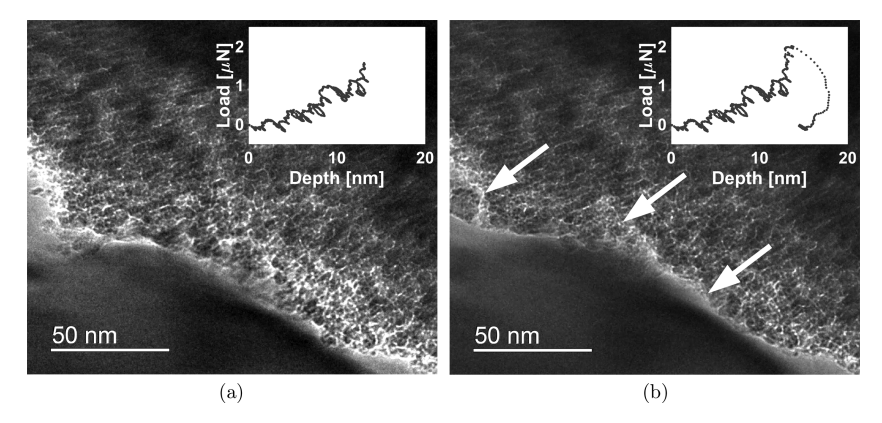


Figure 5. Two frames of a video from an indentation experiment performed *in situ* under the beam of a transmission electron microscope, viewed from the side, (a) before and (b) after a load drop occurs. In the inset force curve of part b, the load drop is visible at right. The silicon substrate is in the top right behind the inset, the diamond indenter is in the bottom left, and the nanoparticle film is in the center. The arrows point to locations where rearrangements, corresponding with the load drop, are visible.

power-law relationship suggests that the relaxation events exhibit a fractal structure. 22,24 This fractal structure of the relaxation events in turn suggests that the material may also exhibit a fractal structure, where rearrangements may occur between individual constituents or between clusters of constituents. In the present system, the activation volume is sufficiently small that only constituent-level rearrangements may be probed. Therefore, it is likely that only the high-magnitude cutoff is observed and any power-law distribution that might exist at a larger scale is not observed here.

Figure 4a shows a topography scan taken prior to indentation experiments. By comparing this image with its counterpart taken after indentations are performed, the extent of plastic deformation can be observed. We carefully correlate the two scans to correct for drift and subtract to observe the portions of the film that rearrange as described previously. Figure 4b shows one such difference image. The plastically deformed region is limited to approximately 20 nm across, which suggests that only one or two particles have been perturbed. Deformation limited to such a small region is consistent with the occurrence of one or two T1 events, especially because the material is quite porous. By contrast, an STZ typically consists of multiple particles, typically moving in several directions 15,16,43 which may be expected to induce pileup. We see no evidence that a single load drop event corresponds to motion of multiple neighboring particles on the

surface, in the region shown in Figure 4b or in many other regions in the film. The depths of these load drop events were typically less than 3 nm, which is less than the diameter of even the smallest particles, which further demonstrates that the rearrangements are limited to only a handful of particles. A few load drop events correspond with displacements as great as 8 nm, which is comparable to the particle diameter. A rearrangement of only two or three particles may have some properties of both the STZ and the T1 process.

In order to better observe the rearrangements, we performed a similar experiment in situ under the beam of a TEM. Two frames from a video (available as Supporting Information) of these experiments are shown in Figure 5, along with the force curve before and after a load drop occurs. A rearrangement about 60 nm across is visible in the center of the image. This rearrangement corresponds with the load drop of 2.3 μ N, which is visible in the inset in Figure 5b. The slight recoil toward the bottom of the load drop occurs because the experiment is performed in displacement control, but the controller does not respond quickly enough to prevent overshoot when such a load drop occurs. The spatial extent of the rearrangement, as observed in the micrograph, indicates that it more closely matches the STZ picture of rearrangements than the T1 process; it may even be large enough to constitute a system-spanning, avalanche-like rearrangement of multiple particles. Due to the larger contact area, the magnitude of this

load drop is much greater than the maximum load ever applied in AFM-based nanoindentation experiments in this study. Nevertheless, these in situ experiments also exhibit a roughly exponential distribution, as shown in the Supporting Information (Figure S6); the decay length is much larger, on the order of 140-180 nN. This larger decay length may be due to the larger contact area, or to the increased mechanical noise present in this system. In the in situ system, the root-meansquare of the mechanical noise out of contact is approximately 200 nN, whereas for the AFM, it is only 0.5 nN. The vibration of the apparatus also serves to nucleate plastic rearrangements, and this dynamic effect combined with the larger contact area are likely responsible for the greater decay length. Nonetheless, the *in situ* experiments demonstrate that load drops correspond with small particle-level rearrangements rather than any other mechanism of plasticity.

Although the present experiments violate some assumptions of the Oliver and Pharr model associated with small deformation, 38,39 we can nevertheless estimate the elastic modulus for the AFM-based experiments using eq 1. The probe is modeled using a spherical area function, and the contact depth is evaluated according to ref 39 as we reported previously. In those cases where the indentation depth is greater than the radius of the AFM tip, the contact area is taken to be a circle with the same radius as the indenter. This is a reasonable approximation because the tip is approximately cylindrical above the hemispherical end. We note that with this analysis, we are unable to appropriately account for sink-in: because the indentation depth is greater than the probe radius, the contact area is unchanged regardless of the choice of ε in eqs 2–3 of ref 39.

Making the assumptions stated above, and given that the radius of this tip is 23 nm, we evaluate a reduced elastic modulus of 11 ± 4 GPa at high humidity. The reduced modulus reached a maximum value of 19 ± 7 GPa at 18% humidity, which was the lowest humidity we were able to attain with the current apparatus. These values are significantly greater than the values we previously determined for silica nanoparticle packings. As those silica nanoparticle films are believed to be more densely packed than the present films, we attribute this stiffening primarily to the rougher geometry of these crystalline particles. The softening at higher humidity may be attributed to the formation of larger liquid domains, which eventually merge and no longer benefit from surface tension, and from the shielding of adhesion forces brought about by the introduction of the liquid phase.

LbL assembled disordered packings of titania and nano-diamond nanoparticles exhibit localized plastic deformation events during indentation which are similar to those reported previously for other disordered materials. The magnitudes and distributions of these load drops follow a roughly exponential distribution, which shares similarity with the upper-magnitude tail of an avalanche distribution. The number of load drops that occur at a given indentation site varies with the relative humidity, with the material being weaker at higher humidity. At very high humidity, the capillary bridges become continuous and the material behaves as a thick colloidal slurry. We are able to observe the motion of particles in both AFM-based and *in situ* TEM-based nanoindentation experiments.

Our results suggest that the mechanical response of the LbL assembled disordered nanoparticle packings may depend on the relative humidity of the environment. These data suggest

that the material system may not be well suited for applications where mechanical stress may be applied while near saturation humidity, because the packing is not structurally stable. However, this transition may be useful in reshaping or molding disordered nanoparticle packings into different shapes or patterns on a surface. Future research may focus on distinctions in the magnitude and spatial extent of rearrangements that occur in disordered materials, as varied by tuning the humidity. Conventional nanoindentation could also be employed to determine whether the trends observed here at the nanoscale can be replicated in indentation experiments at higher load and with greater contact area.

ASSOCIATED CONTENT

S Supporting Information

The Supporting Information is available free of charge on the ACS Publications website at DOI: 10.1021/acs.nanolett.8b01640.

Electron micrograph of an AFM probe after use for nanoindentation at high humidity, an example of a force curve collected at high humidity, comparison topography scans collected under saturated and unsaturated environmental conditions, a Rutherford backscattering spectrum used to determine the porosity of the film, the force curve corresponding to the indentation experiment depicted in Figure 4b, and the distribution of load drop magnitudes resulting from *in situ* TEM nanoindentation experiments (PDF)

Video of a TEM nanoindentation experiment (AVI)

AUTHOR INFORMATION

Corresponding Author

*(R.W.C.) E-mail: carpick@seas.upenn.edu. Telephone: +1 (215) 898-4608. Fax: +1 (215) 573-6334.

ORCID 🏻

Joel A. Lefever: 0000-0003-3423-9661 Jyo Lyn Hor: 0000-0002-0340-8330 Daeyeon Lee: 0000-0001-6679-290X Robert W. Carpick: 0000-0002-3235-3156

Present Address

[∞]Joel A. Lefever: Department of Mechanical Engineering, Union College, Schenectady, NY 12308, United States

Notes

The authors declare no competing financial interest.

ACKNOWLEDGMENTS

The authors thank James Pressly for help with the Rutherford backscattering experiments and Brandon McClimon for help in interpreting the data. Use of the facilities of the Nano/Bio Interface Center and the Nanoscale Characterization Facility at the University of Pennsylvania are acknowledged. We acknowledge support by the UPENN MRSEC, NSF Grant No. DMR-1720530, as well as partial support from NSF Grant No. CMMI-1662695, DMR-1120901, and the Ashton Foundation (J.A.L.).

REFERENCES

- (1) Manning, M. L.; Liu, A. J. Phys. Rev. Lett. 2011, 107, 108302.
- (2) Zhang, L.; Feng, G.; Zeravcic, Z.; Brugarolas, T.; Liu, A. J.; Lee, D. ACS Nano 2013, 7, 8043-8050.

(3) Cubuk, E. D.; Schoenholz, S. S.; Rieser, J. M.; Malone, B. D.; Rottler, J.; Durian, D. J.; Kaxiras, E.; Liu, A. *Phys. Rev. Lett.* **2015**, *114*, 108001.

- (4) Lee, D.; Rubner, M. F.; Cohen, R. E. Nano Lett. 2006, 6, 2305–12.
- (5) Park, J. T.; Kim, J. H.; Lee, D. Nanoscale 2014, 6, 7362-68.
- (6) Park, I.; Ko, S. H.; Pan, H.; Grigoropoulos, C. P.; Pisano, A. P.; Fréchet, J. M. J.; Lee, E. S.; Jeong, J. H. *Adv. Mater.* **2008**, *20*, 489–496
- (7) Cook, K. T.; Tettey, K. E.; Bunch, R. M.; Lee, D.; Nolte, A. J. ACS Appl. Mater. Interfaces 2012, 4, 6426-6431.
- (8) Lefever, J. A.; Jacobs, T. D. B.; Tam, Q.; Hor, J. L.; Huang, Y.-R.; Lee, D.; Carpick, R. W. *Nano Lett.* **2016**, *16*, 2455–2462.
- (9) Lettington, A. H. Carbon 1998, 36, 555-560.
- (10) Ferrari, A. C. Surf. Coat. Technol. 2004, 180-181, 190-206.
- (11) Inoue, A.; Wang, X. M.; Zhang, W. Reviews on Advanced Materials Science 2008, 18, 1-9.
- (12) Leroch, S.; Wendland, M. Langmuir 2013, 29, 12410-12420.
- (13) Strickland, D. J.; Huang, Y.-R.; Lee, D.; Gianola, D. S. Proc. Natl. Acad. Sci. U. S. A. 2014, 111, 18167–72.
- (14) Zeng, J. F.; Chu, J. P.; Chen, Y. C.; Volland, A.; Blandin, J. J.; Gravier, S.; Yang, Y. *Intermetallics* **2014**, 44, 121–127.
- (15) Argon, A. S. Acta Metall. 1979, 27, 47-58.
- (16) Schall, P.; Weitz, D. A.; Spaepen, F. Science 2007, 318, 1895-1899
- (17) Zhou, Y.; Milner, S. T. Soft Matter 2015, 11, 2700-2705.
- (18) Silbert, L. E.; Liu, A. J.; Nagel, S. R. Phys. Rev. Lett. **2005**, 95, 098301
- (19) Liu, A. J.; Nagel, S. R. Annu. Rev. Condens. Matter Phys. 2010, 1, 347–369.
- (20) Cubuk, E. D.; et al. Science 2017, 358, 1033-1037.
- (21) Liu, Y. H.; Wang, D.; Nakajima, K.; Zhang, W.; Hirata, A.; Nishi, T.; Inoue, A.; Chen, M. W. Phys. Rev. Lett. 2011, 106, 125504.
- (22) Denisov, D. V.; Lörincz, K. A.; Uhl, J. T.; Dahmen, K. A.; Schall, P. Nat. Commun. 2016, 7, 10641.
- (23) Uhl, J. T.; et al. Sci. Rep. 2015, 5, 16493.
- (24) Karimi, K.; Ferrero, E. E.; Barrat, J.-L. Phys. Rev. E: Stat. Phys., Plasmas, Fluids, Relat. Interdiscip. Top. 2017, 95, 013003.
- (25) Mitarai, N.; Nori, F. Adv. Phys. 2006, 55, 1-45.
- (26) Herminghaus, S. Adv. Phys. 2005, 54, 221-261.
- (27) Gallego-Gómez, F.; Morales-Flórez, V.; Blanco, Á.; de la Rosa-Fox, N.; López, C. Nano Lett. 2012, 12, 4920-4924.
- (28) Grof, Z.; Lawrence, C. J.; Štěpánek, F. J. Colloid Interface Sci. 2008, 319, 182–192.
- (29) Scheel, M.; Seemann, R.; Brinkmann, M.; Di Michiel, M.; Sheppard, A.; Breidenbach, B.; Herminghaus, S. *Nat. Mater.* **2008**, *7*, 189–193.
- (30) Li, Q.; Tullis, T. E.; Goldsby, D.; Carpick, R. W. Nature 2011, 480, 233-236.
- (31) Liu, Y.; Szlufarska, I. Phys. Rev. Lett. 2012, 109, 186102.
- (32) Schuh, C. A.; Lund, A. C.; Nieh, T. G. Acta Mater. 2004, 52, 5879–5891.
- (33) Packard, C. E.; Schuh, C. A. Acta Mater. 2007, 55, 5348-5358.
- (34) Li, W.; Bei, H.; Tong, Y.; Dmowski, W.; Gao, Y. F. Appl. Phys. Lett. 2013, 103, 171910.
- (35) Lee, D.; Gemici, Z.; Rubner, M. F.; Cohen, R. E. Langmuir 2007, 23, 8833–8837.
- (36) Lee, D.; Omolade, D.; Cohen, R. E.; Rubner, M. F. Chem. Mater. 2007, 19, 1427-1433.
- (37) Jacobs, T. D. B.; Wabiszewski, G. E.; Goodman, A. J.; Carpick,R. W. Rev. Sci. Instrum. 2016, 87, 013703.
- (38) Oliver, W. C.; Pharr, G. M. J. Mater. Res. 1992, 7, 1564-1583.
- (39) Oliver, W. C.; Pharr, G. M. J. Mater. Res. 2004, 19, 3-20.
- (40) Farr, R. S.; Groot, R. D. J. Chem. Phys. 2009, 131, 244104.
- (41) Bi, D.; Zhang, J.; Chakraborty, B.; Behringer, R. P. Nature **2011**, 480, 355–358.
- (42) Vinutha, H. A.; Sastry, S. Nat. Phys. 2016, 12, 578-583.
- (43) Tanguy, A.; Leonforte, F.; Barrat, J. L. Eur. Phys. J. E: Soft Matter Biol. Phys. 2006, 20, 355-364.